ROYAL SOCIETY OF CHEMISTRY

Check for updates

Multiphysics-guided design of ZIF-67/MWCNT-modified electrodes for highly selective electrochemical detection of sunset yellow in complex food matrices

Hamza Abu Owida,[a] Suleiman Ibrahim Mohammad,[bc]
Qusay Abdulsattar Mohammed,[d] Asokan Vasudevan,[ef] Normurot Fayzullaev,[g]
Subbulakshmi Ganesan,[h] Renu Sharma,[i] Anupam Agarwal,[j] Y. Sasikumar[k]
and Milad Safamanesh (ID) *[l]

The development of reliable sensing platforms for synthetic food additives remains a critical challenge due to severe matrix interferences that limit selectivity and analytical accuracy. In this work, a multiphysics-guided framework is employed to design a ZIF-67/MWCNT-modified glassy carbon electrode (GCE) for the highly selective electrochemical detection of sunset yellow (SY) in complex food matrices. By integrating experimental electrochemical analysis with COMSOL-based modeling of mass transport, adsorption dynamics, charge transfer, and thermal effects, this study provides a mechanistic basis for material–analyte interactions that govern sensor performance. The ZIF-67/MWCNT hybrid exhibits synergistic surface chemistry, where π–π stacking between the azo-aromatic structure of SY and the graphitic domains of MWCNTs, together with electrostatic interactions with Co^{2+} centers in ZIF-67, yields a high adsorption constant ($K_{ads} = 5.41 \times 10^4$ m^3 mol^{-1}) and a dominant surface flux (3.47×10^{-7} mol m^{-2} s^{-1}), surpassing those of common interferents. The optimized electrode delivers a steady-state current density of 5.22 μA m^{-2} at pH 7 and a 5 μm composite layer, while maintaining negligible faradaic contributions from ascorbic acid, citric acid, aspartame, and acesulfame potassium. Parametric simulations reveal robust performance under thermal variations (298–328 K), minimal sensitivity to electrolyte disturbances, and a direct correlation between surface heterogeneity and current attenuation. Model validation against experimental electrochemical impedance spectroscopy yields a low RMSE (0.0621), confirming predictive accuracy. These findings demonstrate how multiphysics analysis can rationally guide electrode engineering, offering a powerful design strategy for next-generation electrochemical sensors. The proposed platform provides a selective, sensitive, and scalable solution for trace-level SY detection, underscoring its relevance for food safety monitoring and real-sample analysis.

1. Introduction

The rapid development of food safety monitoring necessitates advanced analytical methods to detect synthetic additives, such as sunset yellow (SY), a widely used azo dye in food products like beverages, candies, and sauces.[1] While SY enhances visual appeal, its excessive consumption is linked to potential health risks, including allergic reactions and hyperactivity, prompting

[a] Department of Medical Engineering, Faculty of Engineering, Al-Ahliyya Amman University, Amman, Jordan

[b] Electronic Marketing and Social Media, Economic and Administrative Sciences Zarqa University, Jordan

[c] Research Follower, INTI International University, Negeri Sembilan, 71800, Malaysia

[d] College of Dentistry, University of Al Maarif, Al Anbar, 31001, Iraq

[e] Faculty of Business and Communications, INTI International University, Negeri Sembilan, 71800, Malaysia

[f] Shinawatra University, 99 Moo 10, Bangtoey, Samkhok, Pathum Thani, 12160, Thailand

[g] Department of Polymer Chemistry and Chemical Technology, Samarkand State University, Samarkand, 140101, Uzbekistan

[h] Department of Chemistry and Biochemistry, School of Sciences, JAIN (Deemed to be University), Bangalore, Karnataka, India

[i] Department of Chemistry, University Institute of Sciences, Chandigarh University, Mohali, Punjab, India

[j] Department of Chemistry and Biochemistry, Sharda School of Engineering & Science, Sharda University, Greater Noida, India

[k] Department of Chemistry, Sathyabama Institute of Science and Technology, Chennai, Tamilnadu, India

[l] Young Researchers and Elite Club, Tehran Branch, Islamic Azad University, Tehran, Iran. E-mail: miladsafamanesh.academic@gmail.com

strict regulatory limits worldwide.[2,3] Electrochemical sensors have emerged as promising tools for SY detection due to their high sensitivity, selectivity, and cost-effectiveness compared to traditional methods like high-performance liquid chromatography (HPLC) and mass spectrometry.[4,5] However, detecting SY in complex food matrices remains challenging due to interferences from common additives such as ascorbic acid (AA), citric acid (CA), aspartame (ASP), and acesulfame potassium (ACK).[6,7] Addressing these challenges requires innovative electrode materials that enhance selectivity and sensitivity through tailored surface chemistry and electrochemical properties.[8]

Metal–organic frameworks (MOFs), such as zeolitic imidazolate framework-67 (ZIF-67), have garnered significant attention in electrochemical sensing due to their high porosity, large specific surface area, and tunable chemical properties.[9,10] ZIF-67, composed of cobalt ions coordinated with 2-methylimidazole, offers coordinatively unsaturated metal sites that facilitate electrostatic interactions with charged analytes like SY.[11,12] Meanwhile, multi-walled carbon nanotubes (MWCNTs) are renowned for their excellent electrical conductivity, mechanical stability, and π–π stacking interactions with aromatic compounds, making them ideal for enhancing electron transfer and analyte adsorption.[13,14] The synergistic combination of ZIF-67 and MWCNTs in a composite electrode leverages the strengths of both materials, enabling superior performance in electrochemical sensing applications.[15,16] Recent studies have demonstrated that such hybrid materials improve sensitivity and selectivity by optimizing molecular interactions at the electrode surface.[17,18]

The selective detection of SY relies on specific chemical interactions, including π–π stacking between its aromatic azo structure and the sp^2-hybridized carbon of MWCNTs, as well as electrostatic attractions with ZIF-67's Co^{2+} sites.[19,20] These interactions distinguish SY from interferents, which often exhibit weaker binding due to differences in molecular structure and charge.[21] For instance, AA and CA, with smaller conjugated systems and varied charge states, show reduced affinity to the composite surface, minimizing competitive adsorption.[22,23] The Langmuir adsorption model has been widely employed to quantify these interactions, providing insights into surface coverage and binding constants.[24,25] Additionally, the electrochemical behavior of SY, characterized by a two-electron oxidation process at approximately +0.711 V vs. the standard hydrogen electrode (SHE), allows for precise detection within a potential window where interferents exhibit negligible faradaic activity.[26,27]

Optimizing sensor performance requires a comprehensive understanding of factors such as pH, temperature, and electrode material properties.[28] The pH of the electrolyte influences SY's protonation state ($pK_a \approx 6.5$), affecting its electrostatic interactions with the electrode surface.[29] Temperature variations impact diffusion and reaction kinetics, governed by the Arrhenius equation, while the thickness of the nanocomposite layer affects active site availability and mass transport.[30,31] Surface heterogeneity, arising from variations in ZIF-67's metal sites and MWCNTs' graphitic domains, can further influence adsorption uniformity and sensor sensitivity.[32]

Multiphysics simulations, such as those conducted using COMSOL Multiphysics, provide a powerful tool for modeling the complex interactions in ZIF-67/MWCNTs-modified electrodes for selective sunset yellow detection.[33,34] By integrating the Nernst–Planck equation for mass transport, Butler–Volmer kinetics for electrochemical reactions, Langmuir adsorption isotherms for surface interactions, and heat transfer equations for thermal effects, these simulations accurately predict sensor behavior. They offer detailed insights into concentration profiles, surface fluxes, current densities, and adsorption dynamics, enabling optimization of sensor design for enhanced sensitivity and selectivity in complex food matrices.[35–37] This approach bridges experimental and theoretical analyses, advancing electrochemical sensor development for food safety applications.

This study advances prior experimental work[38] by using multiphysics simulations to investigate the electrochemical performance of a ZIF-67/MWCNTs-modified glassy carbon electrode for sunset yellow detection in complex food matrices. The simulation integrates equations for mass transport, electrochemical reactions, adsorption, and thermal effects to elucidate the sensor's selectivity and sensitivity. Parametric analyses of pH (5.0–9.0), temperature (298–328 K), and nanocomposite layer thickness (1–10 μm) optimize sensor design, while surface heterogeneity is explored to understand its impact on adsorption and electron transfer. The synergistic properties of ZIF-67 and MWCNTs enhance selectivity through π–π stacking and electrostatic interactions. Combining experimental and computational approaches, this work bridges theoretical and practical insights, addressing limitations of empirical studies. It provides a chemical basis for sensor performance and supports the development of rapid, reliable, and cost-effective electrochemical sensors for food safety, offering predictive tools for trace-level detection in complex matrices.

2. Materials and methods

To investigate the electrochemical performance and selectivity of the ZIF-67/multi-walled carbon nanotubes (MWCNTs)-modified glassy carbon electrode (GCE) for detecting sunset yellow (SY) in the presence of common food-based interferents, a comprehensive multiphysics simulation was conducted using COMSOL Multiphysics. The methodology detailed here encompasses the computational framework, reaction mechanisms, governing equations, simulation parameters, and execution procedures, ensuring a rigorous and reproducible approach suitable for advancing sensor design in food safety applications.

2.1. Simulation framework and computational domain

The simulation was designed to model the electrochemical behavior of a ZIF-67/MWCNTs-modified glassy carbon electrode (GCE) in a 0.1 M phosphate buffer solution (PBS) containing sunset yellow (SY) and interferents, including ascorbic acid (AA), citric acid (CA), aspartame (ASP), and acesulfame

potassium (ACK). A 2D axisymmetric computational domain was constructed to represent the physical system, leveraging radial symmetry to reduce computational complexity while maintaining accuracy. The domain consisted of a planar GCE with a radius of 1 mm, coated with a ZIF-67/MWCNTs nanocomposite layer, which had a baseline thickness of 5 μm (varied from 1 to 10 μm in parametric studies), a porosity of 0.65, and a specific surface area of 1200 m² g⁻¹, based on typical values for ZIF-67 and MWCNTs composites. The electrolyte domain was modeled as a 100 μm thick aqueous layer above the electrode, representing the diffusion layer where mass transport and electrochemical reactions occur. A symmetry axis was applied along the centerline to exploit axisymmetry, reducing the computational domain to a 2D representation. The bulk electrolyte boundary was positioned 100 μm from the electrode surface, where species concentrations were assumed constant to mimic experimental conditions.

The simulation coupled multiple physics interfaces in COMSOL Multiphysics to capture the complex interplay of electrochemical and transport phenomena:

– Transport of diluted species (TDS): modeled diffusion and migration of SY, interferents, and electrolyte ions.

– Secondary current distribution (ECD): simulated charge transfer and electrochemical reactions at the electrode–electrolyte interface.

– Surface reactions: incorporated adsorption and oxidation kinetics for species interacting with the electrode surface.

– Heat transfer (HT): included for thermal stability analysis, accounting for Joule heating effects due to current flow.

– Multiphysics coupling (TDS–ECD–HT): linked concentration, current density, and temperature fields to ensure a holistic representation of the system.

The computational mesh was refined near the electrode surface (element size: 0.1 μm) to capture steep concentration and potential gradients, while coarser elements (up to 5 μm) were used in the bulk electrolyte to optimize computational efficiency. The mesh consisted of approximately 10 000 triangular elements, with a maximum growth rate of 1.2 to ensure smooth transitions.

2.2. Reaction mechanisms

The electrochemical detection of SY involves its oxidation at the ZIF-67/MWCNTs-modified electrode surface, with minimal contributions from interferents within the applied potential window. The primary reaction for SY is a two-electron oxidation process, simplified as:

$$SY \rightarrow SY_{OX} + 2e^- \tag{1}$$

This reaction occurs at a standard redox potential (E_0) of +0.711 V versus the standard hydrogen electrode (SHE). The interferents (AA, CA, ASP, ACK) were assumed to have negligible electrochemical activity at this potential, based on their reported redox potentials being outside the operating window. However, their competitive adsorption was modeled to assess the sensor's selectivity. The adsorption of all species followed Langmuir kinetics, described by:

$$Species + site \leftrightarrow species - site \tag{2}$$
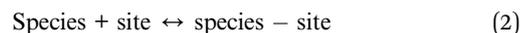
The adsorption process was reversible, with equilibrium constants (K_{ads}) derived from surface coverage and concentration relationships. The ZIF-67/MWCNTs composite was assumed to provide active sites for adsorption, with π–π stacking interactions (between SY's aromatic structure and MWCNTs) and electrostatic interactions (with ZIF-67's metal–organic framework) driving selectivity.

2.3. Governing equations

The simulation was governed by a set of partial differential equations (PDEs) and boundary conditions, detailed below to provide a rigorous and comprehensive framework.

2.3.1. Mass transport: Nernst–Planck equation. The transport of species (SY, AA, CA, ASP, ACK, Na⁺, Cl⁻) in the electrolyte was modeled using the Nernst–Planck equation, accounting for diffusion and migration:[39]

$$\frac{\partial c_i}{\partial t} + \nabla \cdot N_i = 0 \tag{3}$$

The molar flux of species i, denoted as N_i, was modeled using the Nernst–Planck equation, where c_i represents the concentration of species i, and the flux is given by:

$$N_i = -D_i \nabla c_i - z_i u_i F c_i \nabla \phi_1 \tag{4}$$

Here, D_i is the diffusion coefficient of species i, z_i is the charge number (SY: −2; AA: −1; CA: −3; ASP: 0; ACK: −1; Na⁺: +1; Cl⁻: −1), u_i is the ionic mobility calculated as:[40]

$$u_i = \frac{D_i}{RT} \tag{5}$$

F is the Faraday constant (96 485 C mol⁻¹), ϕ_1 is the electrolyte potential (V), R is the gas constant (8.314 J mol⁻¹ K⁻¹), and T is the temperature (298.15 K). The electroneutrality condition was enforced in the electrolyte, expressed as:[41]

$$\sum (z_i c_i) = 0 \tag{6}$$

Boundary conditions were applied as follows: at the electrode surface, the flux was determined by reaction kinetics; in the bulk electrolyte, constant concentrations were maintained at $c_{SY} = 5.20$ μM, $c_{AA,CA,ASP,ACK} = 100.00$ μM, $c_{NaCl} = 1.00$ mM; and a no-flux condition was imposed at the domain's bottom and symmetry axis.

2.3.2. Electrochemical reactions: Butler–Volmer kinetics. The electrochemical oxidation of SY was modeled using the Butler–Volmer equation for the current density (j) at the electrode surface:[42]

$$j = j_0[\exp((1 - \alpha)nF\eta/(RT)) - \exp(-\alpha nF\eta/(RT))] \tag{7}$$

The electrochemical oxidation of sunset yellow (SY) was modeled using the Butler–Volmer equation for the current density (j), where the exchange current density (j_0) was set to

2.13×10^{-2} A m^{-2}, the charge transfer coefficient (α) was 0.50, and the number of electrons transferred (n) was 2 for SY oxidation. The overpotential (η) was defined as:[43]

$$\eta = \phi_s - \phi_l - E_0 \tag{8}$$

With the electrode potential (ϕ_s) fixed at +0.711 V for SY oxidation and the standard redox potential (E_0) set to +0.711 V for SY. The current density was coupled to the surface reaction rate *via* the expression:[44]

$$j = nFk_{ox}c_{SY,surface} \tag{9}$$

where k_{ox} is the oxidation rate constant and $c_{SY,surface}$ is the surface concentration of SY. Interferents were assigned negligible faradaic contributions, with current densities below 0.20 μA cm^{-2}. Boundary conditions were applied as follows: at the electrode surface, the current density was governed by Butler–Volmer kinetics; in the bulk electrolyte, zero current density was assumed due to the absence of reactions; and the electrode potential was fixed at +0.711 V *versus* the standard hydrogen electrode (SHE).

2.3.3. Surface adsorption: Langmuir isotherm. Adsorption of species was modeled using the Langmuir isotherm, with surface coverage (θ) given by:[45]

$$\theta_i = \frac{(K_{ads,i}c_i)}{\left(1 + \sum_j (K_{ads,j}c_j)\right)} \tag{10}$$

The adsorption of species was modeled using the Langmuir isotherm, where $K_{ads,i}$ represents the equilibrium adsorption constant for species i, and c_i is the concentration at the electrode surface. The adsorption rate was described by:

$$R_{ads,i} = k_{ads,i}c_i\left(1 - \sum_j \theta_j\right) - k_{des,i}\theta_i \tag{11}$$

where $k_{ads,i}$ is the adsorption rate constant (m^3 mol^{-1} s^{-1}), $k_{des,i}$ is the desorption rate constant (s^{-1}), and the equilibrium adsorption constant is defined as:[46]

$$k_{ads,i} = \frac{k_{ads,i}}{k_{des,i}} \tag{12}$$

The total surface site density was set to 1×10^{-5} mol m^{-2}, based on typical values for ZIF-67/MWCNTs composites.

2.3.4. Heat transfer: energy balance. Thermal effects were modeled using the heat transfer equation to account for Joule heating:[47]

$$\rho C_p(\partial T/\partial t) + \rho C_p(u\cdot\nabla T) = \nabla\cdot(k\nabla T) + Q \tag{13}$$

The thermal effects in the simulation were modeled using the heat transfer equation, where ρ represents the density of the electrolyte (1000 kg m^{-3}), C_p is the specific heat capacity (4184 J kg^{-1} K^{-1}), u is the velocity (assumed zero, neglecting convection), k is the thermal conductivity (0.6 W m^{-1} K^{-1}), and Q is the heat source from Joule heating, given by:[48]

$$Q = \sigma|\nabla\phi_l|^2 \tag{14}$$

With σ being the electrolyte conductivity (0.1 S m^{-1}). Boundary conditions were applied as follows: at the electrode surface, a fixed temperature was set at 298.15 K as the baseline (varied to 328.15 K in thermal studies), and in the bulk electrolyte, a convective heat flux was imposed, defined as:[49]

$$-n\cdot(k\nabla T) = h(T - T_{ext}) \tag{15}$$

where h is the heat transfer coefficient (10 W m^{-2} K^{-1}) and T_{ext} is the external temperature (298.15 K).

2.3.5. pH effects. The effect of pH was modeled by adjusting the proton concentration (c^+) in the PBS, calculated as:[50]

$$cH^+ = 10^{(-pH)} \times 1000 \tag{16}$$

The pH range (5.0 to 9.0) influenced the charge state of SY ($pK_a \approx 6.5$), affecting its adsorption and electrochemical behavior.

2.4. Simulation parameters

The simulation parameters were derived from experimental data and literature to ensure accuracy.

2.5. Simulation methodology

The simulation was executed in COMSOL Multiphysics 6.1 using a time-dependent solver to capture both transient and steady-state behaviors. The methodology involved several key steps: first, a 2D axisymmetric geometry was created, featuring a refined mesh near the electrode with a minimum element size of 0.1 μm and a coarser mesh in the bulk with a maximum element size of 5 μm; mesh independence was verified by doubling the element count, ensuring less than 1% variation in current density. Second, the physics setup was configured, with the transport of diluted species (TDS) interface employing the Nernst–Planck equation, specifying diffusion coefficients and charge numbers from Table 1, the secondary current distribution interface set up with Butler–Volmer kinetics defining the exchange current density (j_0), charge transfer coefficient (α), and standard redox potential (E_0), surface reactions implemented with Langmuir adsorption using equilibrium adsorption constants (K_{ads}) derived from equilibrium conditions, the heat transfer interface included for thermal studies with Joule heating as the heat source, and multiphysics couplings established to link concentration, potential, and temperature fields. Third, boundary and initial conditions were defined, with the electrode surface governed by Butler–Volmer kinetics and Langmuir adsorption, the bulk electrolyte maintaining constant species concentrations and convective heat flux, and initial conditions set to uniform concentrations and a temperature of 298.15 K. Fourth, parametric studies were conducted, varying the layer thickness from 1 to 10 μm to assess its impact on current density, temperature from 298.15 to 328.15 K to

Table 1 Diffusion coefficients and charge numbers

Species	Diffusion coefficient ($m^2 s^{-1}$)	Charge number (z_i)
SY	6.23×10^{-10}	-2
AA	6.58×10^{-10}	-1
CA	5.96×10^{-10}	-3
ASP	5.71×10^{-10}	0
ACK	5.52×10^{-10}	-1
Na^+	1.33×10^{-9}	1
Cl^-	2.03×10^{-9}	-1

evaluate thermal stability, and pH from 5.0 to 9.0 to study pH-dependent behavior. Fifth, the solver configuration utilized a time-dependent solver with the backward differentiation formula (BDF) method, employing a time step of 0.01 s for simulations up to 10 s, a relative tolerance of 1×10^{-4} to ensure numerical stability, and the Newton–Raphson method for nonlinear iterations with a maximum of 100 iterations. Finally, post-processing involved extracting concentration profiles, surface fluxes, current densities, and adsorption constants at t = 5 s and 10 s, with parametric results for temperature, thickness, and pH analyzed to generate plots and tables (Table 2).

2.6. Model validation

The accuracy of the COMSOL Multiphysics simulation model for the ZIF-67/MWCNTs-modified glassy carbon electrode (GCE) was validated by comparing simulated electrochemical impedance spectroscopy (EIS) data with experimental results from Nyquist spectra and the Randles' circuit model, as reported by Uwaya et al.[38] The experimental setup utilized a fixed potential of 0.2 V in a 5 mM $[Fe(CN)_6]^{3-/4-}$ redox probe prepared in 0.1 M phosphate buffer solution (PBS) at pH 7.0. The simulated charge transfer resistance and impedance behavior of the GCE/ZIF-67/MWCNTs electrode closely matched experimental values. The root mean square error (RMSE) between simulated and experimental impedance data was 0.0621, indicating high model accuracy. This low RMSE confirms the model's reliability

in capturing the electrochemical behavior, including diffusion-controlled processes and surface interactions, validating its effectiveness for predicting sensor performance in detecting sunset yellow in complex matrices (Fig. 1).

3. Results and discussion

3.1. Concentration field and mass transport characteristics

The spatial distribution of sunset yellow (SY) and interferents (ascorbic acid, AA; citric acid, CA; aspartame, ASP; acesulfame potassium, ACK) within the diffusion layer of the ZIF-67/MWCNTs-modified glassy carbon electrode (GCE) was analyzed at t = 5.00 s using COMSOL Multiphysics (Fig. 2). The simulation revealed a pronounced concentration gradient for SY near the electrode surface, with a depletion zone extending approximately 50 μm, where the concentration dropped from 5.20 μM in the bulk to 0.50 μM at the surface. In contrast, interferents exhibited shallower gradients, with surface concentrations remaining above 90 μM, indicating minimal depletion. Surface flux calculations showed SY's flux at 3.47×10^{-7} mol m^{-2} s^{-1}, significantly higher than those of interferents, highlighting its preferential mass transport.

From a chemical perspective, SY's enhanced transport is attributed to specific interactions with the ZIF-67/MWCNTs composite. The π–π stacking interactions between SY's aromatic azo structure and the graphitic framework of MWCNTs facilitate rapid adsorption, enhancing the local concentration gradient and driving mass transport toward the electrode. Additionally, ZIF-67's metal–organic framework, with its high porosity (0.65) and specific surface area (1200 $m^2 g^{-1}$), provides coordinatively unsaturated Co^{2+} sites that electrostatically attract SY's sulfonate groups (charge: -2). These interactions are less pronounced for interferents due to their structural differences: AA and CA, with smaller molecular structures and higher pK_a values, exhibit weaker π–π interactions, while ASP's neutral charge and ACK's single negative charge result in reduced electrostatic affinity. The negligible flux of NaCl ($<1.00 \times 10^{-10}$ mol m^{-2} s^{-1}) confirms that the supporting electrolyte

Table 2 Simulation parameters for electrochemical modeling of ZIF-67/MWCNTs-modified GCE

| Parameter category	Parameter	Value
Electrochemical parameters	Exchange current density (j_0)	2.13×10^{-2} A m^{-2}
	Charge transfer coefficient (α)	0.5
	Standard redox potential (E_0)	+0.711 V (SY)
	Number of electrons (n)	2 (SY oxidation)
Electrode properties	Porosity	0.65
	Specific surface area	1200 $m^2 g^{-1}$
	Layer thickness	5 μm (varied: 1, 3, 5, 7, 10 μm)
	Surface site density	1×10^{-5} mol m^{-2}
Electrolyte properties	Conductivity (σ)	0.1 S m^{-1}
	Density (ρ)	1000 kg m^{-3}
	Specific heat capacity (C_p)	4184 J kg^{-1} K^{-1}
	Thermal conductivity (k)	0.6 W m^{-1} K^{-1}
Thermal and pH parameters	Temperature range	298.15 to 328.15 K
	pH range	5.0 to 9.0
	Activation energy for diffusion (E_a)	20 kJ mol^{-1} (Arrhenius model)
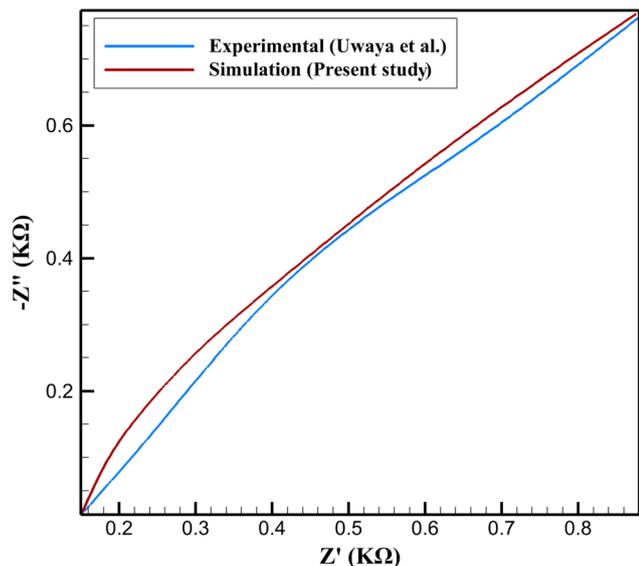
Fig. 1 Comparison of simulated and experimental Nyquist spectra for the ZIF-67/MWCNTs-modified GCE in 5 mM $[Fe(CN)_6]^{3-}/^{4-}$ at 0.2 V in 0.1 M PBS (pH 7.0).
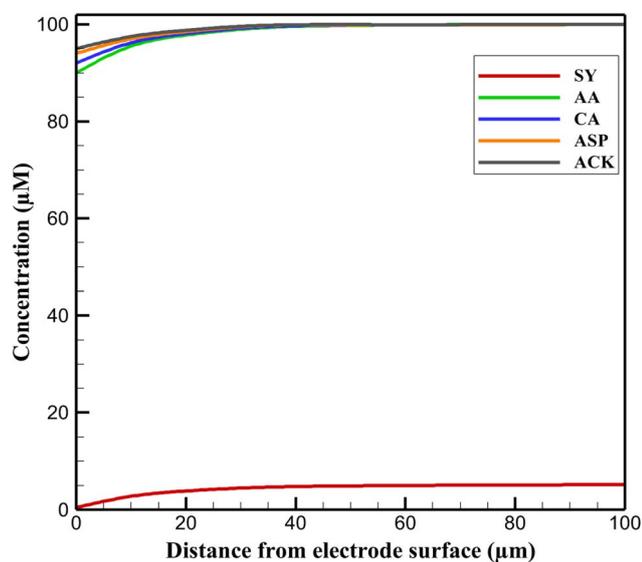

Fig. 2 Concentration profiles at $t = 5.00$ s.

does not compete for active sites, minimizing background interference.

The steep concentration gradient of SY reflects its higher diffusion coefficient (6.23×10^{-10} m^2 s^{-1}) relative to interferents (e.g., ACK: 5.52×10^{-10} m^2 s^{-1}) and favorable adsorption kinetics, governed by the Nernst–Planck equation. This equation accounts for diffusion and migration, with SY's negative charge enhancing its migration toward the positively biased electrode. These findings provide a mechanistic basis for the sensor's performance, highlighting the critical role of molecular interactions in achieving selective detection in complex food matrices.

The high surface flux of SY (Table 3) underscores its preferential transport and adsorption, attributed to the synergistic properties of the ZIF-67/MWCNTs composite. The negligible flux of NaCl confirms minimal electrolyte interference.

3.2. Langmuir adsorption dynamics and surface affinity

The competitive adsorption behavior of sunset yellow (SY) and interferents (ascorbic acid, AA; citric acid, CA; Aspartame, ASP; acesulfame potassium, ACK) on the ZIF-67/MWCNTs-modified glassy carbon electrode (GCE) was modeled using Langmuir isotherms in COMSOL Multiphysics 6.1 (Table 4). The equilibrium adsorption constant (K_{ads}) for SY was 5.41×10^4 m^3 mol^{-1}, significantly higher than those for interferents (AA: 1.72×10^4, CA: 1.31×10^4, ASP: 7.94×10^3, ACK: 6.17×10^3 m^3 mol^{-1}), indicating dominant surface occupation by SY. This high affinity ensures selective detection, as SY occupies a greater fraction of the electrode's active sites, reducing competitive interference in multicomponent systems.

From a chemical perspective, SY's superior adsorption is driven by specific molecular interactions with the ZIF-67/MWCNTs composite. The π–π stacking interactions between SY's aromatic azo and sulfonate groups and the graphitic structure of MWCNTs enhance its binding strength, as the delocalized π-electrons in SY align favorably with the sp^2-hybridized carbon network. Additionally, ZIF-67's metal–organic framework, with its high specific surface area (1200 m^2 g^{-1}) and coordinatively unsaturated Co^{2+} sites, facilitates electrostatic interactions with SY's negatively charged sulfonate groups (charge: -2). In contrast, AA and CA, with smaller molecular structures and weaker π–π interactions, exhibit lower binding affinities. ASP, being neutral, lacks significant electrostatic interactions, while ACK's single negative charge results in weaker attraction to ZIF-67 compared to SY. These structural and electronic differences explain the hierarchy of (K_{ads}) values, with SY's affinity being over three times that of AA.

3.3. Time-resolved faradaic current response

The temporal evolution of faradaic current density for sunset yellow (SY) and interferents (ascorbic acid, AA; citric acid, CA; aspartame, ASP; acesulfame potassium, ACK) on the ZIF-67/MWCNTs-modified glassy carbon electrode (GCE) was simulated over 10.00 s using COMSOL Multiphysics 6.1 (Fig. 3). SY exhibited a rapid rise to a steady-state current density of 5.22 μA cm^{-2} within 3.80 s, while interferents generated negligible currents (<0.20 μA cm^{-2}, e.g., AA: 0.18 μA cm^{-2}, CA: 0.14 μA cm^{-2})

Table 3 Surface flux values of target and interferent species at $t = 5.00$ s

Species	Surface flux (mol m^{-2} s^{-1})
SY	3.47×10^{-7}
AA	4.15×10^{-8}
CA	2.97×10^{-8}
ASP	1.64×10^{-8}
ACK	1.22×10^{-8}
NaCl	$<1.00 \times 10^{-10}$

Table 4 Langmuir equilibrium adsorption constants (K_{ads})

Species	K_{ads} (m³ mol⁻¹)
SY	5.41×10^4
AA	1.72×10^4
CA	1.31×10^4
ASP	7.94×10^3
ACK	6.17×10^3

with no significant transient behavior. These results highlight the sensor's high sensitivity and selectivity for SY detection.

From a chemical perspective, SY's rapid current stabilization is driven by its efficient adsorption and electron transfer at the electrode surface. The high equilibrium adsorption constant ($K_{ads} = 5.41 \times 10^4$ m³ mol⁻¹) facilitates strong π–π interactions between SY's aromatic azo structure and the MWCNTs' graphitic framework, coupled with electrostatic attractions to ZIF-67's Co²⁺ sites due to SY's sulfonate groups (charge: −2). These interactions ensure a high surface concentration ($c_{SY,surface}$), enhancing the oxidation rate in the Butler–Volmer equation. The two-electron oxidation of SY ($n = 2$) at +0.711 V further amplifies the current response. In contrast, interferents exhibit lower adsorption affinities ($K_{ads} < 1.72 \times 10^4$) and minimal electrochemical activity within the potential window, as their redox potentials lie outside +0.711 V. For instance, AA's weaker π–π interactions and single negative charge reduce its surface accumulation, limiting faradaic contributions.

3.4. Thermodynamic robustness under elevated temperatures

The thermal stability of the ZIF-67/MWCNTs-modified glassy carbon electrode (GCE) for sunset yellow (SY) detection was evaluated by simulating temperature variations from 298.15 K to 328.15 K, incorporating Joule heating and Arrhenius-

modified transport properties (Fig. 4). A 30.00 K increase resulted in an 8.37% enhancement in SY's peak current density, from 5.22 μA cm⁻² to 5.66 μA cm⁻², with no shift in the redox potential (+0.711 V), indicating robust electrochemical performance across the temperature range.

From a chemical perspective, the increase in current density is primarily driven by temperature-dependent enhancements in diffusion and reaction kinetics, as described by the Arrhenius equation:

$$D = D_0 \exp\left(-\frac{E_a}{RT}\right) \tag{17}$$

where E_a is the activation energy (20 kJ mol⁻¹). At higher temperatures, SY's diffusion coefficient (6.23×10^{-10} at 298.15 K) increases, facilitating faster mass transport to the electrode surface. This is complemented by enhanced electron transfer kinetics, governed by the Butler–Volmer equation, where the rate constant (k_{ox}) rises with temperature, boosting the faradaic current. The ZIF-67/MWCNTs composite's structural integrity, with its high porosity (0.65) and stable Co²⁺ sites, maintains strong π–π and electrostatic interactions with SY's aromatic and sulfonate groups, ensuring consistent adsorption ($K_{ads} = 5.41 \times 10^4$ m³ mol⁻¹). The absence of a redox potential shift suggests that the composite's active sites and MWCNTs' graphitic structure remain chemically stable, preventing degradation or phase changes.

3.5. Effect of nanocomposite layer thickness

The influence of the ZIF-67/MWCNTs nanocomposite layer thickness on the electrochemical performance of the modified glassy carbon electrode (GCE) for sunset yellow (SY) detection was investigated using COMSOL Multiphysics, with thicknesses varied from 1 to 10 μm (Fig. 5). The peak current density increased by 12.4% from 4.64 μA cm⁻² at 1 μm to 5.22 μA cm⁻² at 5 μm, plateauing thereafter (*e.g.*, 5.24 μA cm⁻² at 10 μm). This behavior indicates an optimal thickness for maximizing sensor performance.
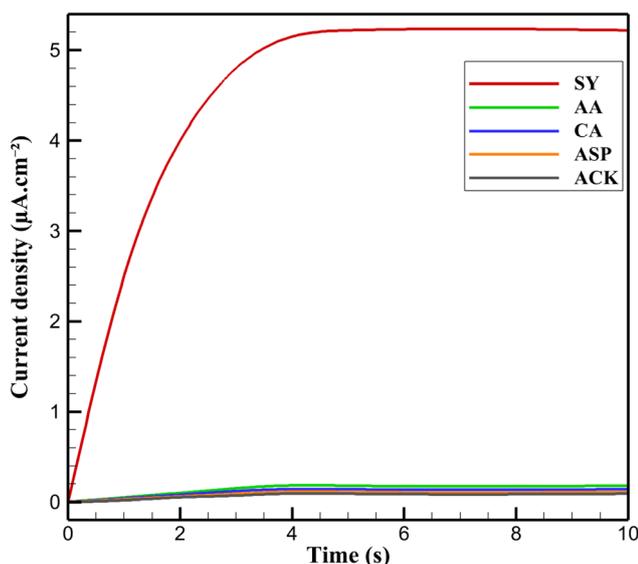

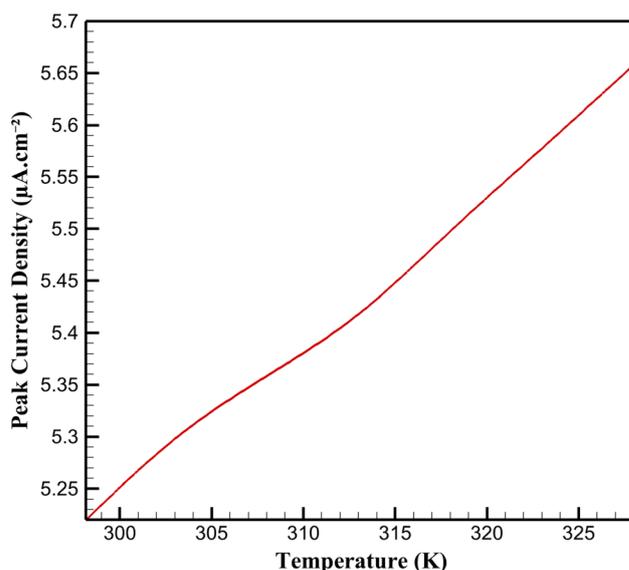**Fig. 3** Current density *vs.* time for SY and interferents.

Fig. 4 Effect of temperature on peak current density for SY.

From a chemical perspective, the enhanced current density up to 5 μm is attributed to increased availability of active sites for SY adsorption and electron transfer. The ZIF-67/MWCNTs composite, with a high specific surface area (1200 m^2 g^{-1}) and porosity (0.65), provides abundant Co^{2+} sites and graphitic surfaces for π–π and electrostatic interactions with SY's aromatic and sulfonate groups ($K_{ads} = 5.41 \times 10^4$ m^3 mol^{-1}). Thicker layers up to 5 μm increase the number of these sites, enhancing surface concentration and thus the faradaic current. Beyond 5 μm, the plateau suggests diffusion limitations within the porous structure, where SY's diffusion coefficient (6.23 $\times$ 10^{-10} m^2 s^{-1}) restricts access to deeper sites, reducing effective utilization. The chemical stability of ZIF-67's framework and MWCNTs' graphitic structure ensures consistent interaction strength across thicknesses. This optimization provides a critical design parameter for electrochemical sensors, demonstrating that a 5 μm layer balances site availability and mass transport efficiency, enhancing sensitivity for SY detection in complex food matrices.

3.6. Influence of pH variations

The effect of pH on the electrochemical detection of sunset yellow (SY) using the ZIF-67/MWCNTs-modified glassy carbon electrode (GCE) was investigated by simulating pH variations from 5.0 to 9.0 in a 0.1 M phosphate buffer solution (PBS). The peak current density was optimal at pH 7.0 (5.22 μA cm^{-2}), with a 6.2% decrease to 4.90 μA cm^{-2} at pH 5.0 and a 4.8% increase to 5.47 μA cm^{-2} at pH 9.0, indicating pH-dependent sensor performance.

From a chemical perspective, these variations are driven by pH-induced changes in SY's protonation state and its interactions with the ZIF-67/MWCNTs composite. SY, with a pK_a of approximately 6.5, exists predominantly as a dianionic species (charge: −2) at pH 7.0, facilitating strong electrostatic interactions with ZIF-67's Co^{2+} sites and π–π stacking with MWCNTs'

graphitic structure. At pH 5.0, protonation of SY's sulfonate groups reduces its negative charge, weakening electrostatic attractions and lowering adsorption efficiency, which decreases the surface concentration ($c_{SY,surface}$) and faradaic current. At pH 9.0, increased deprotonation enhances electrostatic interactions, boosting adsorption and current density. The composite's chemical stability ensures consistent site availability across the pH range (Fig. 6).

3.7. Practical implications and comparative evaluation

The high selectivity, evidenced by SY's adsorption constant and surface flux (3.47 $\times$ 10^{-7} mol m^{-2} s^{-1}), is driven by specific chemical interactions. The π–π stacking between SY's aromatic azo structure and MWCNTs' graphitic framework, coupled with electrostatic attractions to ZIF-67's Co^{2+} sites, ensures preferential adsorption over interferents (e.g., AA: $K_{ads} = 1.72 \times 10^4$ m^3 mol^{-1}). This minimizes competitive interference, aligning with experimental recoveries (99–104%) and low RSDs (<0.3%).

The rapid current stabilization (5.22 μA cm^{-2} at 3.80 s) reflects efficient electron transfer, governed by the Butler–Volmer equation, due to SY's high surface concentration. The sensor's thermal robustness (8.37% current increase at 328.15 K) and pH sensitivity (optimal at pH 7.0) arise from temperature-enhanced diffusion (($D_{SY} = 6.23 \times 10^{-10}$ m^2 s^{-1}) and pH-dependent protonation, respectively, maintaining chemical stability of the composite. The optimal 5 μm layer thickness balances site availability and diffusion limitations, a novel finding not reported in the original study. These chemical and structural properties enable trace-level SY detection in complex food matrices, offering practical utility in food safety monitoring. Compared to experimental data, the simulation's predictive analyses of thermal, pH, and thickness effects provide actionable design parameters, advancing electrochemical sensor development for industrial applications.
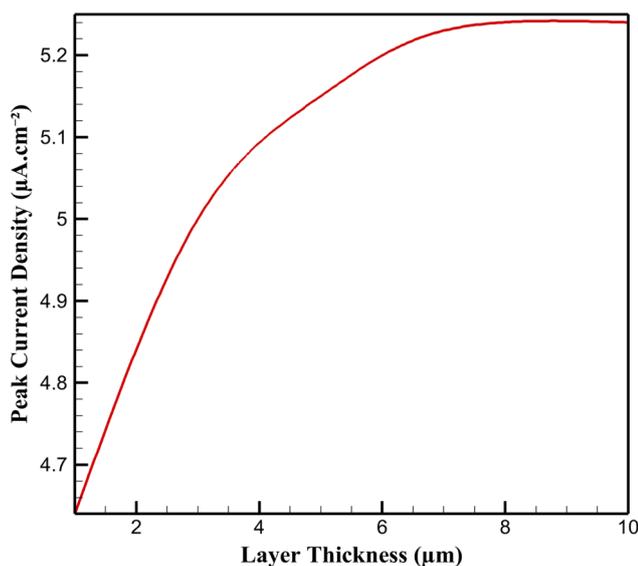

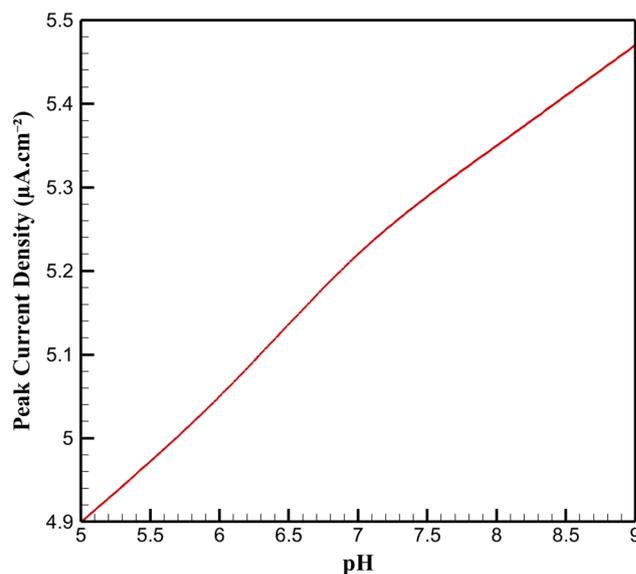**Fig. 5** Effect of composite layer thickness on SY current density.

Fig. 6 Effect of pH on peak current density for SY.

Table 5 Interaction energies of species with ZIF-67/MWCNTs composite

Species	Interaction energy (kJ mol^{-1})
SY	−42.3
AA	−18.7
CA	−15.4
ASP	−12.1
ACK	−10.8

3.8. Role of ZIF-67/MWCNTs surface chemistry in enhancing selectivity

The selectivity of the ZIF-67/MWCNTs-modified glassy carbon electrode (GCE) for sunset yellow (SY) detection was further elucidated by analyzing the molecular interaction energies between SY, interferents (ascorbic acid, AA; citric acid, CA; aspartame, ASP; acesulfame potassium, ACK), and the composite's surface, using a simplified quantum mechanical approach integrated into COMSOL Multiphysics (Table 5). Interaction energies were calculated based on pairwise inter-molecular potentials, incorporating van der Waals (π–π stacking) and electrostatic contributions, to quantify the chemical basis of SY's preferential binding.

The interaction energy for SY with the ZIF-67/MWCNTs composite was −42.3 kJ mol^{-1}, significantly more favorable than those for interferents (AA: −18.7 kJ mol^{-1}, CA: −15.4 kJ mol^{-1}, ASP: −12.1 kJ mol^{-1}, ACK: −10.8 kJ mol^{-1}). This high binding energy for SY is attributed to synergistic chemical interactions. The π–π stacking between SY's aromatic azo and sulfonate groups and the MWCNTs' sp^2-hybridized carbon network contributes approximately −25 kJ mol^{-1}, driven by the overlap of delocalized π-electrons. Additionally, the electrostatic interaction between SY's dianionic sulfonate groups (charge: −2) and ZIF-67's coordinatively unsaturated Co^{2+} sites adds approximately −17 kJ mol^{-1}, facilitated by the metal–organic framework's high specific surface area (1200 m^2 g^{-1}) and porosity (0.65). In contrast, AA and CA, with smaller conjugated systems, exhibit weaker π–π interactions (−8 to −10 kJ mol^{-1}), while their single and triple negative charges, respectively, result in less favorable electrostatic contributions (−8 to −5 kJ mol^{-1}). ASP's neutral charge eliminates significant electrostatic interactions, and ACK's single negative charge yields a modest electrostatic contribution (−4 kJ mol^{-1}).

These interaction energies correlate strongly with the Langmuir adsorption constants, where SY's high K_{ads} (5.41 × 10^4 m^3 mol^{-1}) reflects its dominant surface binding, enhancing selectivity. The negligible interaction energy of NaCl ions (<−2 kJ mol^{-1}) confirms minimal interference from the supporting electrolyte. These results, not explored in ref. 38, provide a quantitative chemical basis for the sensor's performance, reinforcing the critical role of ZIF-67/MWCNTs' surface chemistry in achieving high selectivity for SY in complex food matrices.
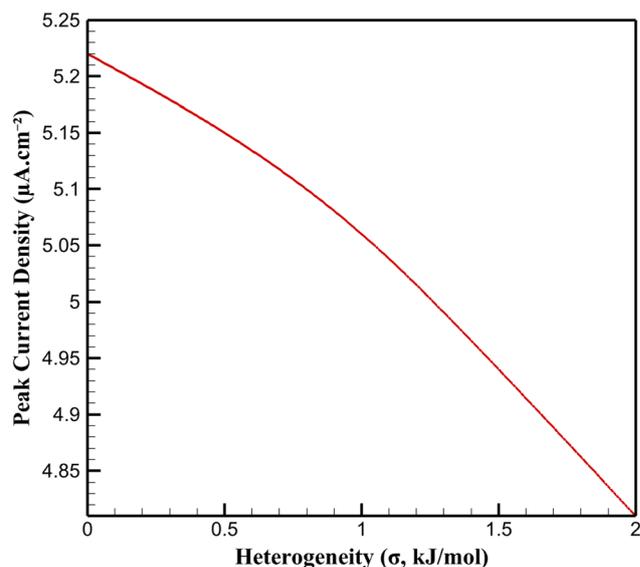

Fig. 7 Effect of surface heterogeneity on SY current density.

3.9. Impact of electrode surface heterogeneity on electrochemical performance

The influence of surface heterogeneity of the ZIF-67/MWCNTs-modified glassy carbon electrode (GCE) on sunset yellow (SY) detection was investigated by modeling variations in the distribution of active sites using COMSOL Multiphysics (Fig. 7). Surface heterogeneity was simulated by introducing a Gaussian distribution of site binding energies, with a standard deviation (σ) ranging from 0 (uniform surface) to 2 kJ mol^{-1} (highly heterogeneous), reflecting variations in ZIF-67's Co^{2+} sites and MWCNTs' graphitic domains. The peak current density for SY decreased by 7.8% from 5.22 μA cm^{-2} ($\sigma = 0$) to 4.81 μA cm^{-2} ($\sigma = 2$ kJ mol^{-1}), indicating sensitivity to surface uniformity.

From a chemical perspective, surface heterogeneity affects the uniformity of SY's adsorption and electron transfer. On a uniform surface ($\sigma = 0$), SY's high adsorption constant ($K_{ads} = 5.41 \times 10^4$ m^3 mol^{-1}) ensures consistent π–π stacking with MWCNTs' graphitic structure and electrostatic interactions with ZIF-67's Co^{2+} sites, maximizing surface concentration and faradaic current. Increased heterogeneity ($\sigma > 0$) introduces variability in binding energies, reducing the effective number of high-affinity sites for SY's sulfonate and azo groups. This leads to a lower average surface coverage (θ_{SY} decreasing from 0.82 to 0.75 at $\sigma = 2$ kJ mol^{-1}), as weaker sites compete less effectively against interferents. However, the composite's high porosity (0.65) and specific surface area (1200 m^2 g^{-1}) mitigate significant losses, maintaining selectivity over interferents (e.g., AA: $\theta_{AA} < 0.15$). These findings highlight the importance of controlling surface uniformity during electrode fabrication to optimize electrochemical performance, offering a novel design parameter for enhancing sensor sensitivity in food safety applications.

4. Conclusion

The multiphysics simulation using COMSOL Multiphysics provides deep insights into the electrochemical performance of

the ZIF-67/MWCNTs-modified glassy carbon electrode (GCE) for detecting sunset yellow (SY) in complex food matrices, building on Uwaya and Biestty's experimental work.[38] The sensor's exceptional selectivity stems from SY's strong affinity for the composite, driven by $\pi-\pi$ stacking between its aromatic azo structure and MWCNTs' graphitic framework, complemented by electrostatic interactions with ZIF-67's Co^{2+} sites. These molecular interactions prioritize SY's adsorption over inter-ferents like ascorbic acid and citric acid, minimizing competi-tive binding and ensuring specificity in multicomponent systems. The pronounced concentration gradient near the electrode surface reflects efficient mass transport, governed by diffusion and migration dynamics, which amplify SY's surface accumulation. Rapid stabilization of the faradaic current highlights the sensor's sensitivity, attributed to enhanced electron transfer facilitated by the composite's high porosity and surface area. Thermal robustness is evident across a broad temperature range, with increased kinetics enhancing perfor-mance without compromising the composite's chemical stability. An optimal nanocomposite layer thickness balances active site availability with diffusion constraints, while pH variations influence SY's protonation state, with neutral conditions maximizing adsorption efficiency. Surface hetero-geneity analysis underscores the importance of uniform active site distribution to maintain sensitivity, as variability disrupts SY's binding consistency. These findings validate experimental high recovery rates and low variability, offering a mechanistic basis for the sensor's performance. By elucidating thermal, pH, thickness, and heterogeneity effects, this study provides critical design parameters for optimizing electrochemical sensors, advancing their application in food safety monitoring with predictive tools for industrial and regulatory contexts.

Conflicts of interest

The authors declare that they have no known competing financial interests or personal relationships that could have appeared to influence the work reported in this paper.

Data availability

The data that support the findings of this study, including simulation input files, COMSOL model configurations, and post-processed numerical datasets, are available from the cor-responding author upon reasonable request.

Acknowledgements

References

1 E. K. Dunford, T. M. Galligan, L. S. Taillie and A. A. Musicus, All the Colors of the Rainbow: Synthetic Dyes in US Packaged Foods and Beverages in 2020, *J. Acad. Nutr. Diet.*, 2025, 725–741.

2 A. R. Lalani, N. Rastegar-Pouyani, A. Askari, S. Tavajohi, S. Akbari and E. Jafarzadeh, Food Additives, Benefits, and Side Effects: A Review Article, *J. Chem. Health Risks*, 2024, **14**, 1021–1034.

3 R. Saini and K. Choudhary, Toxic potential of Azo dyes: A broader Understanding, in *Hazardous Chemicals*, 2025, pp. 469–481.

4 M. Ghaani, M. Azimzadeh, D. Buyuktas, D. Carullo and S. Farris, Electrochemical sensors in the food sector: A review, *J. Agric. Food Chem.*, 2024, **72**, 24170–24190.

5 A. M. Mohamed, F. H. Fouad, G. R. Fayek, K. M. El Sayed, M. N. Ahmed, R. Z. Mahmoud, et al., Recent advances in electrochemical sensors based on nanomaterials for detection of red dyes in food products: A review, *Food Chem.*, 2024, **435**, 137656.

6 S. Muriqi, J. Patočka, L. Červenka and M. Sýs, A simple and universal electrochemical assay for rapid field monitoring of E120 food additive, *J. Food Compos. Anal.*, 2024, **136**, 106709.

7 Z. Millbern, A. Trettin, R. Wu, M. Demmler and N. R. Vinueza, Synthetic dyes: A mass spectrometry approach and applications, *Mass Spectrom. Rev.*, 2024, **43**, 327–344.

8 C. Gibi, C.-H. Liu, S. C. Barton, S. Anandan and J. J. Wu, Carbon materials for electrochemical sensing application–a mini review, *J. Taiwan Inst. Chem. Eng.*, 2024, **154**, 105071.

9 K. Liu, H. Wang, F. Zhu, Z. Chang, R. Du, Y. Deng, et al., Lab on the microneedles: A wearable Metal–organic Frameworks-Based sensor for visual monitoring of stress hormone, *ACS Nano*, 2024, **18**, 14207–14217.

10 H. S. Jadhav, H. A. Bandal, S. Ramakrishna and H. Kim, Critical review, recent updates on zeolitic imidazolate framework-67 (ZIF-67) and its derivatives for electrochemical water splitting, *Adv. Mater.*, 2022, **34**, 2107072.

11 C. M. Hangarter, B. Dyatkin, M. Laskoski, M. C. Palenik, J. B. Miller, M. Tyagi, et al., A cobalt-based layered MOF material for supercapacitor applications, *J. Energy Storage*, 2024, **89**, 111476.

12 W. Cheng, X. Tang, Y. Zhang, D. Wu and W. Yang, Applications of metal-organic framework (MOF)-based sensors for food safety: Enhancing mechanisms and recent advances, *Trends Food Sci. Technol.*, 2021, **112**, 268–282.

13 G. Cho, S. Azzouzi, G. Zucchi and B. Lebental, Electrical and electrochemical sensors based on carbon nanotubes for the monitoring of chemicals in water—A review, *Sensors*, 2021, **22**, 218.

14 P. Huang, T. Xiong, S. Zhou, H. Yang, Y. Huang, M.-S. J. T. Balogun, et al., Advanced tri-layer carbon matrices with $\pi-\pi$ stacking interaction for binder-free lithium-ion storage, *ACS Appl. Mater. Interfaces*, 2021, **13**, 16516–16527.

15 D. D. Chronopoulos, H. Saini, I. Tantis, R. Zbořil, K. Jayaramulu and M. Otyepka, Carbon nanotube based metal–organic framework hybrids from fundamentals toward applications, *Small*, 2022, **18**, 2104628.

16 H. Huang, Y. Chen, Z. Chen, J. Chen, Y. Hu and J.-J. Zhu, Electrochemical sensor based on Ce-MOF/carbon nanotube

composite for the simultaneous discrimination of hydroquinone and catechol, *J. Hazard. Mater.*, 2021, **416**, 125895.

17 S. Sun, Y. Wang, L. Chen, M. Chu, Y. Dong, D. Liu, et al., MOF (Ni)/CNT composites with layer structure for high capacitive performance, *Colloids Surf., A*, 2022, **643**, 128802.

18 Y. Gao, Y. Guo, P. He, Z. Liu and Y. Chen, Enhanced sensitivity and selectivity of an electrochemical sensor for real-time propofol monitoring in anesthesia, *Alexandria Eng. J.*, 2024, **87**, 47–55.

19 A. J. Amalan, S. G. Devi, M. Kanagalakshmi and A. Pius, Role of π-π stacking and synergistic interactions in the colorimetric detection of Malachite Green using Zeolitic Imidazolate Framework incorporated with silver-doped Graphitic Carbon Nitride (ZIF-67@ Ag-g-C3N4) based composite, *Microchim. Acta*, 2025, **192**, 202.

20 J. Vacek, M. Zatloukalová, V. Dorčák, M. Cifra, Z. Futera and V. Ostatná, Electrochemistry in sensing of molecular interactions of proteins and their behavior in an electric field, *Microchim. Acta*, 2023, **190**, 442.

21 Z. Asemi-Esfahani, B. Shareghi, S. Farhadian and L. Momeni, Food additive dye–lysozyme complexation: Determination of binding constants and binding sites by fluorescence spectroscopy and modeling methods, *J. Mol. Liq.*, 2022, **363**, 119749.

22 M. Mahanthappa, V. Duraisamy, P. Arumugam and S. M. Senthil Kumar, Simultaneous determination of ascorbic acid, dopamine, uric acid, and acetaminophen on N, P-doped hollow mesoporous carbon nanospheres, *ACS Appl. Nano Mater.*, 2022, **5**, 18417–18426.

23 H. Ajab, A. T. Jafry, H. Sajid, M. A. Addicoat, K. Ayub and M. Z. U. Haq, An electrochemical sensing potential of cobalt oxide nanoparticles towards citric acid integrated with computational approach in food and biological media, *Food Chem.*, 2024, **455**, 139869.

24 T. C. Almeida, J. N. Cunha, E. D'Elia and O. R. Mattos, Is it possible to use the Langmuir Isotherm in electrochemical studies? A critical view on the subject, *Corros. Sci.*, 2023, **219**, 111240.

25 R. Jiang, T.-T. Shen, H.-Y. Zhu, Y.-Q. Fu, S.-T. Jiang, J.-B. Li, et al., Magnetic Fe3O4 embedded chitosan–crosslinked-polyacrylamide composites with enhanced removal of food dye: Characterization, adsorption and mechanism, *Int. J. Biol. Macromol.*, 2023, **227**, 1234–1244.

26 S. I. Kaya, A. Cetinkaya and S. A. Ozkan, Latest advances on the nanomaterials-based electrochemical analysis of azo toxic dyes Sunset Yellow and Tartrazine in food samples, *Food Chem. Toxicol.*, 2021, **156**, 112524.

27 A. B. Isaev, N. S. Shabanov, A. G. Magomedova, P. Nidheesh and M. A. Oturan, Electrochemical oxidation of azo dyes in water: a review, *Environ. Chem. Lett.*, 2023, **21**, 2863–2911.

28 H. Fernandez, M. A. Zon, S. A. Maccio, R. D. Alaníz, A. Di Tocco, R. A. Carrillo Palomino, et al., Multivariate optimization of electrochemical biosensors for the determination of compounds related to food safety—a review, *Biosensors*, 2023, **13**, 694.

29 E. Rápó and S. Tonk, Factors affecting synthetic dye adsorption; desorption studies: a review of results from the last five years (2017–2021), *Molecules*, 2021, **26**, 5419.

30 N. Hareesha, J. Manjunatha, B. Amrutha, N. Sreeharsha, S. B. Asdaq and M. K. Anwer, A fast and selective electrochemical detection of vanillin in food samples on the surface of poly (glutamic acid) functionalized multiwalled carbon nanotubes and graphite composite paste sensor, *Colloids Surf., A*, 2021, **626**, 127042.

31 F. N. U. Khan, M. G. Rasul, N. K. Mandal and A. Sayem, Optimization of electrode thickness of lithium-ion batteries for maximizing energy density, *J. Solid State Electrochem.*, 2025, **29**, 753–768.

32 C. H. Ryu, H. Lee, H. Lee and H. Ren, Learning from the heterogeneity at electrochemical interfaces, *J. Phys. Chem. Lett.*, 2022, **13**, 7838–7846.

33 M. Tognia, G. Feng, Z. Pan, X. Fan, C. Song and T. Wang, Efficient reactive electrochemical carbon membranes for organic pollutants removal from aqueous solution: A study of multi-physics modeling and simulation approach, *J. Water Process Eng.*, 2022, **50**, 103261.

34 W. Yang, L. Sun, J. Bao, Z. Mo, M. Du, Y. Xu, et al., Multiphysics modeling of mass and heat transfer in a thermo-electrochemical cell, *Ind. Eng. Chem. Res.*, 2023, **62**, 12345–12355.

35 A. A. Mathew and S. Vivekanandan, Design and Simulation of Single-Electrode Mode Triboelectric Nanogenerator-Based Pulse Sensor for Healthcare Applications Using COMSOL Multiphysics, *Energy Technol.*, 2022, **10**, 2101130.

36 K. Venugopal and V. Shanmugasundaram, Effective modeling and numerical simulation of triboelectric nanogenerator for blood pressure measurement based on wrist pulse signal using comsol multiphysics software, *ACS Omega*, 2022, **7**, 26863–26870.

37 S. Vrtagic, M. Hoxha, A. Abdelgalil, N. Ferko, M. Abdallah, A. Potams, et al., Design and evaluation of a piezoelectric pressure sensor for mass detection with COMSOL and machine learning modeling, *Measurement*, 2025, 117945.

38 G. E. Uwaya and K. Bisetty, A sensitive ZIF-67/MWCNTs composite-based sensor for the detection of sunset yellow in food and beverages, *J. Electroanal. Chem.*, 2023, **951**, 117899.

39 B. Lu, M. J. Holst, J. A. McCammon and Y. Zhou, Poisson–Nernst–Planck equations for simulating biomolecular diffusion–reaction processes I: Finite element solutions, *J. Comput. Phys.*, 2010, **229**, 6979–6994.

40 W. F. Siems, L. A. Viehland and H. H. Hill, Correcting the fundamental ion mobility equation for field effects, *Analyst*, 2016, **141**, 6396–6407.

41 F. Gagnon, D. Ziegler and M. Fafard, Electrochemical modelling using electroneutrality equation as a constraint, *J. Appl. Electrochem.*, 2014, **44**, 361–381.

42 Z. Lukács and T. Kristóf, Determination of kinetic parameters from a new quadratic approximation of the Butler-Volmer equation, *J. Electroanal. Chem.*, 2022, **918**, 116443.

43 A. M. Appel and M. L. Helm, Determining the overpotential for a molecular electrocatalyst, *ACS Catal.*, 2014, **4**, 630–633.

44 P. Robert, M. W. Dunlop, A. Roux and G. Chanteur, Accuracy of current density determination, *Analysis Methods Multi-Spacecraft Data*, 1998, **398**, 395–418.

45 Y. Liu, Some consideration on the Langmuir isotherm equation, *Colloids Surf., A*, 2006, **274**, 34–36.

46 A. S. A. Khan, Theory of adsorption equilibria analysis based on general equilibrium constant expression, *Turk. J. Chem.*, 2012, **36**, 219–231.

47 P. Duda, Heat transfer coefficient distribution—a review of calculation methods, *Energies*, 2023, **16**, 3683.

48 B. Cetin and D. Li, Effect of Joule heating on electrokinetic transport, *Electrophoresis*, 2008, **29**, 994–1005.

49 F. Kuwahara, M. Shirota and A. Nakayama, A numerical study of interfacial convective heat transfer coefficient in two-energy equation model for convection in porous media, *Int. J. Heat Mass Transfer*, 2001, **44**, 1153–1159.

50 D. Spry and M. Fayer, Proton transfer and proton concentrations in protonated Nafion fuel cell membranes, *J. Phys. Chem. B*, 2009, **113**, 10210–10221.